1 RAINFALL AND ROCKFALLS IN THE CANARY ISLANDS: ASSESSING A SEASONAL

2 LINK

3 Massimo Melillo[a], Stefano Luigi Gariano[a], Silvia Peruccacci[a], Roberto Sarro[b], Rosa Marìa Mateos[c],

4 Maria Teresa Brunetti[a]

6 [a] CNR IRPI, via Madonna Alta 126, 06128, Perugia, Italia

7 massimo.melillo@irpi.cnr.it, stefano.luigi.gariano@irpi.cnr.it, silvia.peruccacci@irpi.cnr.it

8 [b] IGME, c/ Alenza, 1, 28003, Madrid, España

9 r.sarro@igme.es

10 [c] IGME, Urb. Alcázar del Genil, 4. Edificio Zulema, bajos, 18006, Granada, España

11 rm.mateos@igme.es

13 Correspondence to: Maria Teresa Brunetti maria.teresa.brunetti@irpi.cnr.it

Abstract

Rockfalls are frequent and harmful phenomena occurring in mountain ranges, coastal cliffs and slope cuts. Albeit several natural processes concur in their formation and triggering, rainfall is one of the most common causes. The prediction of rock failures is of social significance for civil protection purposes and can rely on the statistical analysis of past rainfall conditions that caused the failures. The paper describes the analysis of information on rainfall-induced rockfalls in Gran Canaria and Tenerife, Canary Islands (Spain). An analysis of the monthly rainfall versus the monthly distribution of rockfalls reveals that they are correlated for most of the year, except in summer, when other triggers act to induce collapses. National and regional catalogues with hourly and daily rainfall measurements are used to reconstruct the cumulated amount (E) and the duration (D) of the rainfall responsible for the rock failures. Adopting a consolidated statistical approach, new ED rainfall thresholds for possible rockfall occurrence and the associated uncertainties are calculated for the two test sites. As far as is known, this is the first attempt to predict this type of failure using the threshold approach. Using the rainfall information, a map of the mean annual rainfall is obtained for Gran Canaria and Tenerife, and it is used to assess the differences between the thresholds. The results of is study are expected to improve the ability to forecast rockfalls in the Canary Islands, in view of implementing an early warning system to mitigate the rockfall hazard and reduce the associated risk.

Keywords: Rockfall, rainfall threshold, Canary Islands.

1   Introduction

Rockfalls are instability processes affecting mountainous regions, coastal cliffs and slope cuts. Being very rapid, they are extremely dangerous and life-threatening, especially when they occur in populated areas, along roads and railways. The most frequent triggering factors of rockfalls are rainfall, cycling thermal stress, and seismic activity (Wieckzorek and Jaeger, 1996; Keefer, 2002; Mateos, 2016; Ansari et al., 2015; Collins and Stock, 2016; Contino et al., 2017; Sarro et al., 2018; Saroglou, 2019; González de Vallejo et al., 2020). At regional and global scales, empirical approaches to forecast the occurrence of rockfalls may contribute reducing risk. Generally, for rainfall-induced slope failures the forecast can rely upon the definition of rainfall thresholds, i.e. the rainfall conditions that when reached or exceeded are likely to trigger the failure. Rainfall thresholds are calculated through the statistical analysis of historical rainfall conditions that have resulted in landslides (e.g., Guzzetti et al., 2007, 2008; Cepeda et al. 2010; Sengupta et al., 2010; Ruiz-Villanueva et al. 2011; Berti et al., 2012; Staley et al., 2013; Zêzere et al., 2015; Palenzuela et al., 2016; Rosi et al., 2016; Peruccacci et al., 2017; Segoni et al., 2018; Valenzuela et al., 2018, 2019). The definition of reliable empirical rainfall thresholds relies on the use of objective procedures for (i) the reconstruction of the rainfall events responsible for the failures and (ii) the calculation of the thresholds. For the purpose, Melillo et al. (2018) have proposed an algorithm that reconstructs rainfall events, identifies the rainfall conditions that have resulted in slope failures, and calculates probabilistic cumulated event rainfall-rainfall duration (*ED*) thresholds at different non-exceeding probabilities and their associated uncertainties (Peruccacci et al., 2012). The obtained thresholds are a set of parallel power-law curves in a log-log (*D*,*E*) plane, which are characterized by a slope and an intercept, the last being a function of the non-exceeding probability value (Brunetti et al., 2010).

In this work, a relationship between the amount of rainfall and the occurrence of rockfalls is assessed and empirical rainfall thresholds are defined for two test sites in Gran Canaria and Tenerife, Canary Islands (Spain). The possible prediction of rainfall-induced rock failures is of fundamental importance primarily for the safety of the inhabitants and for preserving infrastructures such as roads and buildings. An increasing level of safety against this type of hazard is also important for the local economy, one third of which is based on tourism. As far as is known, this is the first attempt to predict rock failures triggered by rain using the threshold approach. Recently, in Italy it has been observed that the slope of the power-law curve is dependent on the mean annual rainfall (MAR). In particular, the higher is the MAR the steeper is the threshold (Peruccacci et al., 2017). This relationship is explained assuming that where the landscape has been shaped over long time periods by landslides

67 triggered by a given minimum amount of rainfall, it is likely necessary at least as much rainfall to

68 trigger the next landslides (Chen, 2015). For improving the discussion of the results, it has been

69 considered worthwhile producing a map of the MAR for the islands of Gran Canaria and Tenerife

70 using the available rainfall data sets.

71 The manuscript is organized as follows. After a description in Section 2 of the general settings of the

72 two test sites, Section 3 describes the rainfall and rockfall datasets, and the methods used to determine

73 *ED* rainfall thresholds and the map of the MAR. Section 4 illustrates in detail the relationship between

74 the rainfall regime and the occurrence of rock failures, and presents the rainfall thresholds for the

75 possible rockfall occurrence in the two test sites. Finally, in Section 5, the main findings of the work

76 are summarised and discussed.

77 ## 2   Test site description

78 The Canary Islands (Spain) are one of the major volcanic chain in the oceans. The archipelago

79 consists of eight islands in the Atlantic Ocean, aligned along a W-SW to E-NE direction: El Hierro,

80 La Palma, La Gomera, Tenerife, Gran Canaria, Fuerteventura, La Graciosa and Lanzarote. The

81 geological origin of the Canary archipelago (800 km in length) is still under debate, but it has been

82 traditionally interpreted as a hotspot track (Fullea et al., 2015).

83 The steep topography and the geological complexity of the archipelago influence the activation of an

84 intense slope failures activity. Rockfalls are the most frequent landslide type in the Canary Islands,

85 causing damage on built-up areas and communication networks.

86 Two test sites are selected for assessing the relationship between the rainfall and the occurrence of

87 rockfalls. The first site (GC) is located in the north-western part of Gran Canaria island, and the

88 second site (TEN) is the entire Tenerife island (Fig. 1).

89 ### 2.1 Gran Canaria Island (GC-200 road)

90 Gran Canaria is the third island in size of the Canarian archipelago. With an area of 1560 km^2 and a

91 maximum altitude of 1956 m a.s.l., the island is approximately circular in shape (Fig. 1). The origin

92 of Gran Canaria can be dated about 15 million years ago (Miocene) with the first submarine building

93 stages of the Gran Canaria Volcano. From the geological point of view, the island presents the greatest

94 variability of igneous rocks of the entire archipelago. Besides the distinctive lavas of the basanite

95 basalt to trachyte phonolite series, Gran Canaria presents also other types of magma, such as tholeiitic

96   basalts and rhyolites (Troll and Carracedo, 2016). Massive flank failures and erosion give place to

97   chaotic deposits that cover large areas.

98   The test site is the GC-200 road located in the north-western extreme of Gran Canaria, and specifically

99   between the localities of Agaete and Aldea. The road constitutes the main transportation corridor

100 between the two localities. With a length of 34 km, the road path is very tortuous following the

101 contour of the coast, a very step coastline with some of the highest cliffs in Europe. The road has

102 heavy traffic estimated on average at 1500 vehicles per day. The geology of the test site area is within

103 the domain of the basaltic shield stage, Middle Miocene in age. Along the road, an alternance of

104 alkaline basaltic deposits and piroclastic flows can be observed. In some parts, gravitational deposits

105 (mainly colluvial) also outcrop covering wide areas.

106 Regarding climatological conditions, Gran Canaria is located in a transitional zone between temperate

107 and tropical conditions. The conical morphology of Gran Canaria retains the humidity of the

108 predominant N-NE trade winds of the subtropical Azores anticyclone on the north side of the island.

109 As a result, the northern flanks are humid and vegetation is vigorous, while the south part of the island

110 is very dry and the conditions are very arid and desert-like. Annual rainfall ranges between 100 and

111 900 mm on average, increasing with altitude. In the test site the climate is very dry, with low average

112 annual rainfall (< 100 mm) and high average annual temperature (~ 20°C).

113 *2.2 Tenerife island*

114 Tenerife (Fig. 1) is the largest (2057 km^2) and the most populated (950,000 inhabitants and 13.2

115 million visitors in 2019) island of the archipelago. It is home to the third largest volcano in the world

116 (Pico del Teide, 3718 m a.s.l.).

117 From a geological point of view, Tenerife was constructed via Miocene–Pliocene shields that now

118 form the vertices of the island. The shields were unified into a single edifice by later volcanism that

119 continued in central Tenerife from approximately 12 to 8 million years ago and was followed by a

120 period of dormancy. Rejuvenation at approximately 3.5 Ma is recorded by the central Las Cañadas

121 Volcano, and long residence times of magmas during this period favoured magmatic differentiation

122 processes to produce an episode of felsic and highly explosive felsic volcanism (Troll and Carracedo,

123 2016).

124 The steep orography of the island and the climate variety have resulted in a diversity of landscapes

125 and geographical formations. Very impressive coastal cliffs (till 500 m in height) are present in the

126 northern corner of Tenerife. This area is also characterized by narrow and deep ravines which
127 determine an intense slope activity.

128 The climate of Tenerife is subtropical oceanic; the minimum and maximum annual average
129 temperatures are about 15ºC in winter and 24ºC in summer. Similarly to Gran Canaria, annual rainfall
130 ranges between 100 and 900 mm. Tenerife offers a large variety of micro-climate zones controlled
131 by the altitude and the winds.

3   Data and methods

133 The availability of rainfall measurements and landslide information is fundamental to define reliable
134 rainfall thresholds. For the selection of the rain gauges, the data quality and the location of the rain
135 gauges are assessed, given that these features are crucial to characterize the spatial-temporal variation
136 of the precipitations. Similarly, the calculation of the MAR relies on the availability of sufficiently
137 long rainfall series (at least 30 years). This is difficult to achieve for a dense network of rain gauges,
138 where sensors may exhibit different operating time periods. The World Meteorological Organization
139 (WMO) guidelines on the calculation of the annual standard normal, specifically the MAR,
140 recommend at least 10 years to define at least provisional MAR maps (WMO, 1989). This is the case
141 in the test sites, where a lot of rainfall information is limited to short time periods (the average is 15.6
142 years), thus hampering the calculation of the MAR with a detailed space resolution.

3.1 Rainfall data

144 In the GC test site, hourly rainfall data (purple triangles in Fig. 1) from the Spanish National
145 Meteorological Service (AEMET) network (in total 25 stations among which 4 are close to the study
146 area) are used for the calculation of rainfall thresholds. Moreover, daily rainfall data (orange triangles
147 in Fig.1) are provided from the *Consejo Insular de Aguas de Gran Canaria* (CIAGC) regional rain
148 gauge network (13 stations) and from AEMET (92 stations, among which 7 are close to the study
149 area). Some of the sensors of the AEMET network provide both hourly and daily rainfall, in different
150 time periods. Details of the rainfall series are reported in Table 1.

151 For the TEN test site, rainfall measurements are provided by AEMET with the contribution of
152 regional networks. As for the GC test site, the rainfall analysis is performed using both hourly and
153 daily data. The two networks in the TEN test site are composed by 34 rain gauges recording hourly
154 data (purple triangles in Fig. 1) and 66 rain gauges recording daily data (orange triangles in Fig. 1).

155 To calculate the MAR for the two test sites, yearly and monthly rainfall data provided by AEMET

156 and by *Sistema de Información Agroclimático y de Regadíos* (SIAR), respectively, are used (Table

157 1). In particular, in order to obtain homogeneous maps, data recorded in the 20-year period from

158 January 2000 to December 2019 in both test sites are selected. Following WMO guidelines (WMO,

159 1989), only stations with at least 10 years of data are included in the analysis. Overall, 72 (one every

160 22 km^2) and 67 (one every 31 km^2) rain gauges are used to calculate MAR in Gran Canaria and

161 Tenerife, respectively. The average number of sensors operating per year in the considered period is

162 56 (84%; one every 28 km^2) in Grand Canaria and 47 (65%; one every 43 km^2) in Tenerife. The used

163 rain gauges are homogeneously distributed over the test site areas.

164 Using the monthly and annual rainfall data recorded by the 103 rain gauges in the two islands, the

165 MAR for the period 2000-2019 was calculated for each station. Moreover, the coefficient of variation

166 of the MAR is calculated by dividing its standard deviation by the MAR. This coefficient represents

167 the variability of the MAR in the considered time interval. The map of the MAR and of its coefficient

168 of variation are calculated using the tension spline tool in ESRI ArcMAP 10.7.1.

169 ### *3.2 Rockfall data*

170 The information on the rockfalls was collected by the Road Maintenance Service in the GC test site

171 and by the Canarian Civil Protection Authorities in the TEN test site. After a rockfall occurrence, a

172 quick action is required by local authorities to remove boulders from road, and to repair the damage.

173 The average response time for these emergencies is down to one day, and therefore the date of the

174 rockfall occurrence is the same of the road inspection. Figure 2 portrays an example of rockfalls

175 occurred in GC and TEN test sites.

176 For the GC test site a total of 8174 rockfall events occurred from January 2010 to March 2016 was

177 documented. A catalogue was prepared defining accurately the location of each impact along the road

178 using orthophotos available for the region and technical reports. The information for each event

179 includes kilometre point, number of events, date, and boulder size. In GC only 535 rockfalls

180 characterized by medium to large size are included in the analysis for the thresholds, whereas small

181 and very small rockfalls ($< 10^{-3}$ m^3) are discarded. Analogously, a catalogue of 1898 rockfalls that

182 impacted along Tenerife roads from January 2010 to November 2017 was prepared. For each event,

183 the information includes rockfall localization, geographic accuracy, occurrence day, month, year, and

184 time (if available), and temporal accuracy.

185 The influence of the rainfall on the occurrence of rockfalls is assessed analysing the distribution of

186 monthly rainfall (Figs. 3a,b) and monthly number of rockfalls (Figs. 3c,d) on the two test sites. As

187 expected, an increase of the rainfall in the autumn-winter period, between October and March, is

188 observed in both islands, with a maximum in November.

189 The monthly distribution of rockfalls in Gran Canaria (Fig. 3c) is coherent with the rainfall values in

190 the period January-April, with a maximum in February (~ 130; Fig. 3a). For the remaining dry (May

191 to September) and wet (October to December) months the number of rock failures decreases and

192 becomes almost flat (below 50). This behaviour suggests the presence of triggering mechanisms other

193 than the rainfall. For the TEN test site, the number of rockfalls per month (Fig. 3b) is similar to the

194 rainfall distribution, confirming anyway the presence of one or more additional triggers as evidenced

195 by the abundance of failures between May and September (Fig. 3d) when the rainfall is irrelevant.

196 ### 3.3 Empirical rainfall thresholds

197 Empirical *ED* thresholds are represented by the following power law curve:

198 $$E = (\alpha \pm \Delta\alpha) \times D^{(\gamma \pm \Delta\gamma)} \qquad (1)$$

199 where E is the cumulated event rainfall (in mm), D is the duration of the rainfall event (in hours or in

200 days), α and γ are the intercept and the slope of the curve, respectively, and $\Delta\alpha$ and $\Delta\gamma$ are the

201 uncertainties associated with them. Thresholds at different non-exceedance probabilities are

202 calculated adopting the frequentist approach and the bootstrap nonparametric statistical technique

203 (Brunetti et al., 2010; Peruccacci et al., 2012), using 5000 randomly selected synthetic series of *DE*

204 pairs. A threshold at 5% non-exceedance probability should leave 5% of the empirical *DE* pairs below

205 itself. The parameter uncertainties depend mostly on the number and the distribution of the rainfall

206 conditions. The minimum number of *DE* pairs needed for having stable mean values of the parameters

207 α and γ (i.e. reliable thresholds) depends on the distribution and dispersion of the empirical data points

208 in the *DE* domain.

209 ### 3.4 The CTRL-T algorithm for threshold calculation

210 The quantitative identification of the rainfall responsible for slope failures and the definition of

211 reliable thresholds are fundamental steps towards a well-founded event prediction (Peruccacci et al.,

212 2017; Melillo et al., 2018). The use of standardized procedures for the reconstruction of the rainfall

213 conditions able to trigger past failures and for the definition of thresholds is necessary for enhancing

214   the objectivity and reproducibility of the curves. The tool named CTRL-T (Calculation of Thresholds
215   for Rainfall-induced Landslides - Tool) proposed by Melillo et al. (2018) is exploited to calculate *ED*
216   thresholds for the two test sites. CTRL-T reconstructs rainfall events starting from continuous rainfall
217   series. For each rockfall, the algorithm: 1) identifies automatically the representative rain gauge; 2)
218   identifies multiple (*D*,*E*) rainfall conditions responsible for the failure; 3) selects among them the
219   maximum probability rainfall conditions (MPRCs). Then, analysing the distribution of the MPRCs it
220   calculates probabilistic rainfall thresholds at different non-exceeding probabilities and their
221   associated uncertainties. In order to avoid using wrong temporal information (i.e., incorrect dates for
222   the occurrence of rockfalls) in the definition of the thresholds, the rainfall conditions having a delay
223   longer than 48 hours between the rainfall ending time and the rockfall occurrence are discarded.

224   Using CTRL-T, 82 rockfalls occurred between 2012 and 2016 in GC test site and 626 rockfalls
225   occurred between 2010 and 2016 in the TEN test site are selected (light green dots in Fig. 1). The
226   remaining records are discarded due to the: 1) absence of rainfall data in the period including the
227   collapse occurrence time; 2) absence of rain gauges within a buffer of 15 km radius centred on the
228   rockfall; 3) lack of an evident correlation with the rainfall. The definition of rainfall thresholds relies
229   only upon rainfall conditions that triggered the first failure in each event. As a consequence, numerous
230   rockfalls (106, 39% in GC and 271, 30% in TEN) which occurred at the same date and in the same
231   location, and which are associated with the same rainfall event are discarded. In GC among the
232   remaining rockfalls 53 are analysed with daily and 29 with hourly rainfall data, respectively. The low
233   number of rock failures associated to hourly-based rain gauges is to be ascribed to the low density of
234   the sensors in the area, and precludes the definition of rainfall thresholds. In TEN 245 rockfalls are
235   reconstructed with hourly data and 381 with daily rainfall data. Note that for 83 failures it was possible
236   reconstructing the rainfall conditions using sensors from both the two rain gauge networks. As a
237   consequence, the reconstructed (*D*,*E*) rainfall conditions have different temporal resolutions and are
238   used to define both hourly-based and daily-based rainfall thresholds.

239   **4   Results**

240   A correlation between the rainfall and the observed failures is confirmed by the comparison between
241   the monthly rainfall and the corresponding number of rockfalls both in GC and in TEN (Fig. 4).
242   Figures 4a,b,c show the boxplots of cumulated monthly rainfall based on the data recorded in rain
243   gauges used to reconstruct the rainfall responsible for rockfalls for GC and TEN test sites. Inspection
244   of these figures reveals that the rainfall pattern in the two test sites is typically Mediterranean, with a
245   maximum in winter (but also in October and November) and a minimum in summer, with practically

246 no rain in the warmest months. Analysing data from seven daily-based rain gauges in GC (GC-d), it

247 turns out that the rainiest months are February and November with an average rainfall of 52.2 mm

248 and 55.7 mm, a highest rainfall of 98.6 mm and 133.9 mm, and a median rainfall of 42.3 mm and

249 39.8 mm, respectively (Fig. 4a). A similar trend is found for Tenerife using both daily and hourly

250 data. Data from 40 daily-based rain gauges in TEN (TEN-d) are analysed finding an average rainfall

251 of 64.6 mm and 86.4 mm, a highest rainfall of 183.5 mm and 183.6 mm, and a median rainfall of 56.1

252 mm and 93.2 mm for February and November, respectively (Fig. 4b). Data from 21 hourly-based rain

253 gauges in TEN (TEN-h) are analysed finding an average rainfall of 88.8 mm and 82.0 mm, a highest

254 rainfall of 169.8 mm and 190.8 mm, and a median rainfall of 97.5 mm and 66.4 mm for February and

255 November, respectively (Fig. 4c).

256 Figures 4d,e,f portray the monthly number of rockfalls associated with rainfall events for GC-d, TEN-

257 d and TEN-h. The GC catalogue lists 53 collapses occurred in the period from November 2012 to

258 October 2016, with the majority of the failures in 2015 (22). The month with the largest number of

259 rockfalls (14) is February, followed by January (8) and November (7). The least number of failures

260 is reported in September (1) and no rainfall-induced rockfalls are reported in May and July (Fig. 4d).

261 The 245 rock failures in the TEN-d catalogue cover the period from September 2010 to February

262 2016, with the majority of records in 2014 (66). The month with the largest number of rockfalls (80)

263 is November, followed by October (37) and December (36). The least number of failures is reported

264 in May (1) and no rainfall-induced rockfalls are reported in June and July (Fig. 4e). The TEN-h

265 catalogue lists 381 rockfalls occurred in the period from September 2010 to November 2016, with

266 the majority of the failures in 2014 (90). The month with the largest number of rockfalls (115) is

267 November, followed by December (72) and October (64). The least number of failures is reported in

268 May (1) and no collapses are reported in July (Fig. 4f).

269 The rainfall that triggered the rockfalls is classified according to the method proposed by Alpert et al.

270 (2002), based on six daily rainfall (E_d) categories from "light" to "torrential" over the Mediterranean

271 (Table 2). Using the procedure adopted by Melillo et al. (2016), each rainfall condition responsible

272 for rock failures (MPRC) is attributed to a specific category. In particular, for events lasting less than

273 24 hours, a category based on the total cumulated rainfall of the event is assigned. For events lasting

274 more than 24 hours, the maximum value of the cumulated rainfall in 24 hours in a moving window is

275 used. In GC, over 40% of the MPRCs responsible for the collapses are classified as moderate-high

276 (MH); in TEN, approximately 30% as high (H) and high-torrential (HT). No MPRCs are found in the

277 lowest Alpert's category (light, Table 2). Figures 4g,h,i show the cumulated percentage of rainfall

278 events per month grouped according to Alpert's classification. In GC-d, in February (Fig. 4g) 6

279   rockfalls (43%) are triggered by a rainfall classified as H, 3 (21%) as torrential (H), 3 (22%) as MH,

280   and 1 as light-moderate (LM) and HT each (14%). In TEN-d, in November, 29 rockfalls (36%) are

281   triggered by a rainfall classified as HT, 26 (33%) as MH, 22 (28%) as H, 2 (2%) as LM, and 1 (1%)

282   as T (Fig. 4h). In TEN-h, in November, 5 (4%), 26 (23%), 26 (23%), 31 (27%) and 27 (23%) rockfall

283   are triggered by a rainfall classified as LM, MH, H, HT and T, respectively (Fig. 4i).

284   Using the catalogues of rainfall events with rockfalls described above and the CTRL-T tool, *ED*

285   thresholds, and their associated uncertainties are calculated for GC and TEN test sites. Table 3 lists

286   the number of MPRC used to define the thresholds, the equations of the power law curves, and the

287   range of validity for the thresholds, expressed in hours or days. Note that *D* must be expressed in days

288   in the equations for the thresholds calculated with daily data, and in hours in the equations for the

289   thresholds calculated with hourly data (Gariano et al., 2020).

290   Figure 5a shows, in logarithmic coordinates, the distribution of the (*D*,*E*) rainfall conditions,

291   reconstructed with daily data, that have caused rockfalls in GC (53 blue dots) and in TEN (245 green

292   dots). In particular, the 53 daily rainfall conditions responsible for the rockfalls in GC have durations

293   in the range $1 \leq D \leq 11$ days (with an average value of 2 days) and cumulated rainfall in the range

294   $16.5 \leq E \leq 219.9$ mm (average value 51.6 mm). All the conditions were recorded in rain gauges

295   located at a maximum distance of 5.7 km from the failures, with a mean value of 2.8 km. The 245

296   daily-based rainfall conditions associated with the collapses in TEN have durations ranging from one

297   to 15 days, with a mean value of two days. The cumulated rainfall ranges from 15.4 to 235.0 mm,

298   with an average of 71.5 mm. The average distance between the rockfalls and their representative rain

299   gauges is 2.2 km, with a maximum distance of 5 km. Figure 5a portrays also the 5% *ED* thresholds

300   for GC ($T_{5,GC-d}$, blue curve) and TEN ($T_{5,TEN-d}$, green curve). The shaded areas around the threshold

301   lines show the uncertainty regions associated to the thresholds (Table 3). Figure 5b portrays the same

302   $T_{5,GC-d}$ and $T_{5,TEN-d}$, in linear coordinates, in the range $1 \leq D \leq 7$ days.

303   Figure 5c shows, in logarithmic coordinates, the distribution of the (*D*,*E*) rainfall conditions,

304   reconstructed with hourly data, that have triggered rock failures in TEN (381 purple dots). The hourly

305   rainfall conditions associated to rockfalls have durations ranging from 2 to 712 hours and mean value

306   of 111 hours. The cumulated rainfall ranges from 10.6 to 433.9 mm, with an average of 105.6 mm.

307   The average distance between the rockfalls and the representative rain gauges is 6.7 km, with a

308   maximum distance of 14.9 km. In the log-log plot the purple curve is the 5% threshold for TEN

309   ($T_{5,TEN-h}$) obtained with hourly data. Figure 5d portrays the same $T_{5,TEN-h}$, in linear coordinates, in the

310 range $1 \leq D \leq 120$ hours. The uncertainty associated with the threshold (purple shaded area in Figs.
311 5c,d) is also shown.

312 The difference between the $T_{5,GC\text{-}d}$ and $T_{5,TEN\text{-}d}$ thresholds can be ascribed to the different MAR in the
313 two test sites. Figure 6 portrays the maps of the MAR and of its coefficient of variation, which is the
314 percentual variability (standard deviation) of the MAR in the considered time interval. The
315 geographical distribution of the MAR values exhibits the highest values in the northern parts of both
316 islands, where it overcomes 800 mm (Fig. 6a). On the contrary, the highest values of the coefficient
317 of variation (i.e. an index of the MAR variability) are localized in the southern part of the islands,
318 where the rain gauge density is lower (Fig. 6b).

5   Discussion and conclusions

320 In Canary Island rainfall is the most important triggering factor for rockfalls (Fig. 3). Nevertheless,
321 there are other factors that predispose directly or indirectly the trigger of the failure (Temiño et al.,
322 2013a). Factors that greatly accentuate this hazard in the two test sites are wind, geomorphological
323 characteristics (e.g., slope, aspect), type of soil and seismic activity. Regarding the wind many
324 collapses are caused by strong gusts of wind that affect the northern side of Tenerife Island and the
325 road GC-200 from Agaete to Aldea in Gran Canaria. (Temiño et al., 2013b). Regarding the
326 geomorphology, the existence of many sections of road running through the old basaltic massifs with
327 significant sub-vertical jointing, makes the area very susceptible to rock failures. In addition, the
328 action of the trade winds on the higher altitude areas, produces an increase in the relative humidity,
329 as large masses of water vapor are retained by steep slopes resulting in an intense weathering (and
330 weakening) of the rock masses. Finally, the large flank instability of the two test sites (especially in
331 the northwest sector of the Gran Canaria island) could be related to structural control and to seismic
332 activity connected to the dynamic geologic condition that characterizes them. (Masson et al., 2002;
333 Temiño et al. 2013b; Urgeles et al., 2001).

334 By selecting the subset of rockfalls triggered by rainfall it can be observed that their monthly
335 frequency is linked to the monthly distribution of the rainfall measured in nearby rain gauges (Figs.
336 4a-f). For GC-d (Figs. 4a,d) the correlation is apparently weaker in fall than in winter, but this could
337 be ascribed to a statistical fluctuation and should be confirmed by increasing the number of events.
338 Conversely, for TEN-d (Figs. 4b,e) the monthly number of rock failures well reflects the monthly
339 rainfall amount, suggesting that rainfall is the only triggering cause. Hourly rainfall data in TEN-h

340 (Figs. 4c,f) confirm partially this outcome, since even with a median lower amount of rainfall, a

341 higher number of rock failures is expected to occur from October to December than in February.

342 The number of rockfalls for which it has been possible to reconstruct the rainfall conditions (MPRCs)

343 using daily and hourly data in the TEN test site (Figs. 4e,f) is different. This is mostly due to the worst

344 temporal resolution of the TEN-d dataset.

345 In the two test sites, the majority of the rainfall responsible for rockfalls belongs to the Alpert's MH

346 category (Figs. 4g,i). In TEN-h, 31 events belong to the most severe category T, whereas in TEN-d

347 only one event is found in the T category. This result could be ascribed to the time step of the moving

348 window used to assign the Alpert's category. For a rainfall event lasting more than one day, the

349 Alpert's category varies depending on the data temporal resolution, since the time step is one hour or

350 one day for the hourly and daily data, respectively. In TEN-d, the total amount of rainfall responsible

351 for the failure is shared in two or more consecutive days, causing a lowering of the Alpert's category,

352 as confirmed by the paucity of T events in TEN-d.

353 Figure 5 shows that $T_{5,TEN-d}$ is higher and steeper than $T_{5,GC-d}$. This means that, at increasing values

354 of D, a smaller amount of rainfall (E) is necessary to trigger the collapses in GC than in TEN.

355 Comparing Figures 1 and 5, the recorded rockfalls in the TEN test site are localized in areas including

356 several classes of MAR (ranging from 100 to 800 mm), while in GC test site they fall in the area

357 characterized by the lowest class of MAR (≤ 100 mm). The different ranges of MAR values in the

358 two test sites are able to explain the observed differences in the two daily ED thresholds (Fig. 5a).

359 This finding confirms that where the MAR is higher, the minimum rainfall conditions able to trigger

360 a failure, specifically a rockfall, are also higher.

361 Moreover, the threshold defined for the TEN test site has an uncertainty smaller than the threshold

362 for GC test site. Peruccacci et al. (2012) observed that the parameter uncertainty reduces as the

363 number of MPRC used to calculate the threshold increases. In particular, as derived from Table 3, the

364 relative uncertainty of the intercept, $\Delta\alpha/\alpha$ is 9.8% for $T_{5,GC-d}$ and 4.9% for $T_{5,TEN-d}$. Regarding the

365 slope of the curves, $\Delta\gamma/\gamma$ is 16.1% for $T_{5,GC-d}$ and 6.7% for $T_{5,TEN-d}$. Given the lower uncertainty range

366 and relative uncertainties of both parameters, $T_{5,TEN-d}$ has a reliability higher than that of $T_{5,GC-d}$. The

367 same analysis for the $T_{5,TEN-h}$ threshold gives $\Delta\alpha/\alpha = 9.3\%$ and $\Delta\gamma/\gamma = 4.2$. Thresholds with an hourly

368 temporal resolution and having relative uncertainties of the parameters α and γ lower than 10% could

369 be implemented in an operative system for the prediction of rainfall-induced failures (Peruccacci et

370 al., 2012; 2017). The thresholds for different non-exceedance probabilities obtained for TEN test site

371 using hourly rainfall data are suited for the design of probabilistic schemes for the operative prediction
372 of rainfall-induced rockfalls. An improvement in the number of rain gauges providing hourly
373 measurements, as well as in the number of recorded rock failures, would be necessary in GC test site
374 in order to reduce the uncertainty of the threshold.

375 Currently, neither prototype nor operative early warning systems for rainfall-induced failures are
376 present in the Canary Islands (Guzzetti et al. 2020). The findings of this work can contribute to the
377 understanding of the rainfall conditions that can trigger rainfall-induced rockfalls in Tenerife and in
378 the western part of Gran Canaria, and their relationship with mean annual rainfall regime. These
379 findings have scientific and social implications given that in both test sites also spring and autumn
380 are characterized by a moderately occurrence of rock failures, with relevant impacts on the
381 population, tourism activities, and local economy. As long as a sufficient amount of empirical data
382 will be available in both test sites (and also in other islands of the archipelago), the method adopted
383 in this work for the definition of reliable rainfall thresholds can be replicated, and the results can be
384 implemented in a prototype early warning system.

6 Code availability

386 The code of CTRL-T was written using the R open-source software and can be freely downloaded at:
387 http://geomorphology.irpi.cnr.it/tools/rainfall-events-and-landslides-thresholds/ctrl-t-algorithm/ctrl-
388 code/ctrl_t_code.r/view. An example of the input files required by the algorithm can be freely
389 downloaded at: http://geomorphology.irpi.cnr.it/tools/rainfall-events-and-landslides-thresholds/ctrl-
390 t-algorithm/input-demo/INPUT.zip/view.

7 Author contribution

392 All authors designed the experiment and carried it out. M.M., S.P. and M.T.B. developed the model
393 code, R.S. and R.M.M. provided the data, and M.M. and S.L.G. performed the simulations. All
394 authors analyzed the results and prepared the manuscript.

8 Competing interests

396 The authors declare that they have no conflict of interest.

9 Acknowledgements

Research conducted within the framework of the U-Geohaz project (Geohazard Impact Assessment for Urban Areas) funded by the European Commission, Directorate-General Humanitarian Aid and Civil Protection (ECHO), under the call UCPM-2017-PP-AG. This work was also funded by the Salvador de Madariaga Mobility Program from the Spanish Ministry of Science, Project: PRX18/00020 and by the University of Alicante. Authors would also like to thank Dr. Luis E. Hernández Gutiérrez, from the Regional Service of Studies and Ecological Impacts of the Canary Islands Government.

10 References

Alpert, P., Ben-Gai, T., Baharan, A., Benjamini, Y., Yekutieli, D., Colacino, M., Diodato, L., Ramis, C., Homar, V., Romero, R., Michaelides, S., and Manes, A.: The paradoxical increase of Mediterranean extreme daily rainfall in spite of decrease in total values, Geophy. Res. Lett., 29(11), 31-1–31-4, https://doi.org/10.1029/2001GL013554, 2012.

Ansari, M.K., Ahmed, M., Rajesh Singh, T.N., and Ghalayani, I.: Rainfall, a major cause for rockfall hazard along the roadways, highways and railways on hilly terrains in India, in: Lollino, G., Manconi, A., Clague, J., Shan, W., and Chiarle, M. (Eds.) Engineering Geology for Society and Territory – Vol. 1, pp. 457–460, Springer, Cham, https://doi.org/10.1007/978-3-319-09300-0_87, 2015.

Berti, M., Martina, M.L.V., Franceschini, S., Pignone, S., Simoni, A., and Pizziolo, M.: Probabilistic rainfall thresholds for landslide occurrence using a Bayesian approach, J. Geophys. Res, 117, F04006, https://doi.org/10.1029/2012JF002367, 2012.

Brunetti, M.T., Peruccacci, S., Rossi, M., Luciani, S., Valigi, D., and Guzzetti, F.: Rainfall thresholds for the possible occurrence of landslides in Italy, Nat. Hazards Earth Syst. Sci., 10, 447–458, https://doi.org/10.5194/nhess-10-447-2010, 2010.

Cepeda, J., Höeg, K., and Nadim, F.: Landslide-triggering rainfall thresholds: a conceptual framework, Q. J. Eng. Geol. Hydroge., 43, 69–84, https://doi.org/10.1144/1470-9236/08-066, 2010.

Chen, C., Saito, H., and Oguchi, T.: Rainfall intensity–duration conditions for mass movements in Taiwan, Prog. Earth Planet. Sci., 2, 14, https://doi.org/10.1186/s40645-015-0049-2, 2015.

424 Collins, B.D., and Stock, G.M.: Rockfall triggering by cyclic thermal stressing of exfoliation
425 fractures. Nat. Geosci., 9, 395–400, https://doi.org/10.1038/ngeo2686, 2016.

426 Contino, A., Bova, P., Esposito, G., Giuffré, I., and Monteleone, S.: Historical analysis of rainfall-
427 triggered rockfalls: the case study of the disaster of the ancient hydrothermal Sclafani Spa (Madonie
428 Mts, northern-central Sicily, Italy) in 1851, Nat. Hazards Earth Syst. Sci., 17, 2229–2243,
429 https://doi.org/10.5194/nhess-17-2229-2017, 2017.

430 Fullea, J., Camacho, A.G., Negredo, A.M., and Fernández, J.: The Canary Islands hot spot: new
431 insights from 3D coupled geophysical–petrological modelling of the lithosphere and uppermost
432 mantle, Earth Planet. Sci. Lett., 409, 71–88, https://doi.org/10.1016/j.epsl.2014.10.038, 2015.

433 Gariano, S.L., Melillo, M., Peruccacci, S., and Brunetti, M.T.: How much does the rainfall temporal
434 resolution affect rainfall thresholds for landslide triggering?, Nat. Hazards, 100, 655–670,
435 https://doi.org/10.1007/s11069-019-03830-x, 2020.

436 González de Vallejo, L.I.; Hernández-Gutiérrez, L.E.; Miranda, A.; Ferrer, M. Rockfall Hazard
437 Assessment in Volcanic Regions Based on ISVS and IRVS Geomechanical Indices. Geosciences, 10,
438 220–239, https://doi.org/10.3390/geosciences10060220, 2020.

439 Guzzetti, F., Peruccacci, S., Rossi, M., and Stark, C.P.: Rainfall thresholds for the initiation of
440 landslides in central and southern Europe, Meteorol. Atmos. Phys., 98(3), 239–267,
441 https://doi.org/10.1007/s00703-007-0262-7, 2007.

442 Guzzetti, F., Peruccacci, S., Rossi, M., and Stark, C.P.: The rainfall intensity–duration control of
443 shallow landslides and debris flows: an update, Landslides 5(1), 3–17,
444 https://doi.org/10.1007/s10346-007-0112-1, 2008.

445 Guzzetti, F., Gariano, S.L., Peruccacci, S., Brunetti, M.T., Marchesini, I., Rossi, M., and Melillo, M.:
446 Geographical landslide early warning systems, Earth-Sci. Rev., 200, 102973,
447 https://doi.org/10.1016/j.earscirev.2019.102973, 2020.

448 Keefer, D.K.: Investigating landslides caused by earthquakes – A historical review, Surv. Geophys.,
449 23, 473–510, https://doi.org/10.1023/A:1021274710840, 2002.

450   Masson, D.G., Watts, A.B., Gee, M.J.R., Urgeles, R., Mitchell, N.C., Le Bas, T.P., and Canals, M.:
451   Slope failures on the flanks of the western Canary Islands, Earth-Sci. Rev., 57, 1–35,
452   https://doi.org/10.1016/S0012-8252(01)00069-1, 2002.

453   Mateos, R.M., García-Moreno, I., Reichenbach, P., Herrera, G., Sarro, R., Rius, J., and Aguiló, R.:
454   Calibration and validation of rockfall modelling at regional scale: application along a roadway in
455   Mallorca (Spain) and organization of its management, Landslides, 13, 751-763,
456   https://doi.org/10.1007/s10346-015-0602-5, 2016.

457   Melillo, M., Brunetti, M.T., Peruccacci, S., Gariano, S.L., and Guzzetti, F.: Rainfall thresholds for
458   the possible landslide occurrence in Sicily (southern Italy) based on the automatic reconstruction of
459   rainfall events, Landslides, 13(1), 165–172, https://doi.org/10.1007/s10346-015-0630-1, 2016.

460   Melillo, M., Brunetti, M.T., Peruccacci, S., Gariano, S.L., Roccati, A., and Guzzetti, F.: A tool for
461   the automatic calculation of rainfall thresholds for landslide occurrence, Environ. Model. Softw., 105,
462   230–243, https://doi.org/10.1016/j.envsoft.2018.03.024, 2018.

463   Palenzuela, J.A., Jiménez-Perálvarez, J.D., and Chacón, J.: Assessing critical rainfall thresholds for
464   landslide triggering by generating additional information from a reduced database: an approach with
465   examples from the Betic Cordillera (Spain), Nat. Hazards, 84, 185–212,
466   https://doi.org/10.1007/s11069-016-2416-8, 2016.

467   Peruccacci, S., Brunetti, M.T., Luciani, S., Vennari, C., and Guzzetti, F.: Lithological and seasonal
468   control of rainfall thresholds for the possible initiation of landslides in central Italy, Geomorphology,
469   139–140, 79–90, https://doi.org/10.1016/j.geomorph.2011.10.005, 2012.

470   Peruccacci, S., Brunetti, M.T., Gariano, S.L., Melillo, M., Rossi, M., and Guzzetti, F.: Rainfall
471   thresholds for possible landslide occurrence in Italy, Geomorphology, 290, 39–57,
472   https://doi.org/10.1016/j.geomorph.2017.03.031, 2017.

473   Rosi, A., Peternel, T., Jemec-Auflič, M., Komac, M., Segoni, S., and Casagli, N.: Rainfall thresholds
474   for rainfall-induced landslides in Slovenia, Landslides, 13, 1571–1577,
475   https://doi.org/10.1007/s10346-016-0733-3, 2016.

476   Ruiz-Villanueva, V., Bodoque, J.M., Díez-Herrero, A., and Calvo, C.: Triggering threshold
477   precipitation and soil hydrological characteristics of shallow landslides in granitic landscapes,
478   Geomorphology, 133(3), 178–189, https://doi.org/10.1016/j.geomorph.2011.05.018, 2011.

479   Saroglou, C.: GIS-based rockfall susceptibility zoning in Greece, Geosciences, 9(4), 163,
480   https://doi.org/10.3390/geosciences9040163, 2019.

481   Sarro, R., Riquelme, A., García-Davalillo, J., Mateos, R., Tomás, R., and Pastor, J.: Rockfall
482   Simulation Based on UAV Photogrammetry Data Obtained during an Emergency Declaration:
483   Application at a Cultural Heritage Site, Remote Sens., 10(12), 1923,
484   https://doi.org/10.3390/rs10121923, 2108.

485   Segoni, S., Piciullo, L., and Gariano, S.L.: A review of the recent literature on rainfall thresholds for
486   landslide occurrence, Landslides, 15, 1483–1501, https://doi.org/10.1007/s1034 6-018-0966-4, 2018.

487   Sengupta, A., Gupta, S., and Anbarasu, K.: Rainfall thresholds for the initiation of landslide at Lanta
488   Khola in north Sikkim, India, Nat. Hazards, 52, 31–42, https://doi.org/10.1007/s11069-009-9352-9,
489   2010.

490   Staley, D.M., Kean, J.W., Cannon, S.H., Schmidt, K.M., and Laber, J.L.: Objective definition of
491   rainfall intensity–duration thresholds for the initiation of post-fire debris flows in southern California,
492   Landslides, 10, 547–562, https://doi.org/10.1007/s10346-012-0341-9, 2013.

493   Temiño, J.Y., Rodrìguez-Peces, M.J., Marchesini, S., Leyva, S., and Dìaz-Hernàndez, J.L.:
494   Amplification of the destructive effects of rock falls by sliding on volcanic soils: examples from the
495   Anaga Massif (Tenerife Island, Spain), in: Margottini, C., Canuti, P., and Sassa, K. (Eds.) Landslide
496   Science and Practice, Springer-Verlag Berlin Heidelberg, Vol. 1, pp. 191–195,
497   https://doi.org/10.1007/978-3-642-31325-7_25, 2013a.

498   Temiño, J.Y., Rodrìguez-Peces, M.J., Sànchez, N., Galindo, I., and del Potro, R.: Geomorphologic
499   evidences of flank instabilities in the eastern sector of the Tejeda volcano (Canary Islands, Spain)
500   during the Quaternary, in: Margottini, C., Canuti, P., and Sassa, K. (Eds.) Landslide Science and
501   Practice, Springer-Verlag Berlin Heidelberg, Vol. 7, pp. 65–72, https://doi.org/10.1007/978-3-642-
502   31313-4_9, 2013b.

503   Troll, V.R., and Carracedo, J.C.: The Geology of the Canary Islands, Elsevier, pp. 636. ISBN 978-0-
504   12-809663-5, https://doi.org/10.1016/C2015-0-04268-X, 2016.

505   Urgeles, R., Canals, M., and Masson, D.G.: 2001 Flank stability and processes off the western Canary
506   Islands: a review from El Hierro and La Palma, Sci. Mar., 65(1), 21–31,
507   https://doi.org/10.3989/scimar.2001.65s121, 2001.

508   Valenzuela, P., Domínguez-Cuesta, M.J., Mora García, M.A., and Jiménez-Sánchez, M.: Rainfall

509   thresholds for the triggering of landslides considering previous soil moisture conditions (Asturias,

510   NW Spain), Landslides, 15, 273–282, https://doi.org/10.1007/s10346-017-0878-8, 2018.

511   Valenzuela, P., Zêzere, J.L., Domínguez-Cuesta, M.J., and Mora García, M.A.: Empirical rainfall

512   thresholds for the triggering of landslides in Asturias (NW Spain), Landslides, 16, 1285–1300,

513   https://doi.org/10.1007/s10346-019-01170-2, 2019.

514   Wieczorek, G.F., and Jaeger, S.: Triggering mechanisms and depositional rates of postglacial slope

515   movement processes in the Yosemite Valley, California, Geomorphology, 15, 17–31,

516   https://doi.org/10.1016/0169-555X(95)00112-I, 1996.

517   WMO – World Meteorological Organization: Calculation of Monthly and Annual 30-Year Standard

518   Normals, WMO/TD No. 341, WCDP-No. 10, Geneva, 1989.

519   Zêzere, J.L., Vaz, T., Pereira, S., Oliveira, S.C., Marques, R., and Garcia, R.A.C.: Rainfall thresholds

520   for landslide activity in Portugal: a state of the art, Environ. Earth Sci., 73(6), 2917–2936,

521   https://doi.org/10.1007/s12665-014-3672-0, 2015.
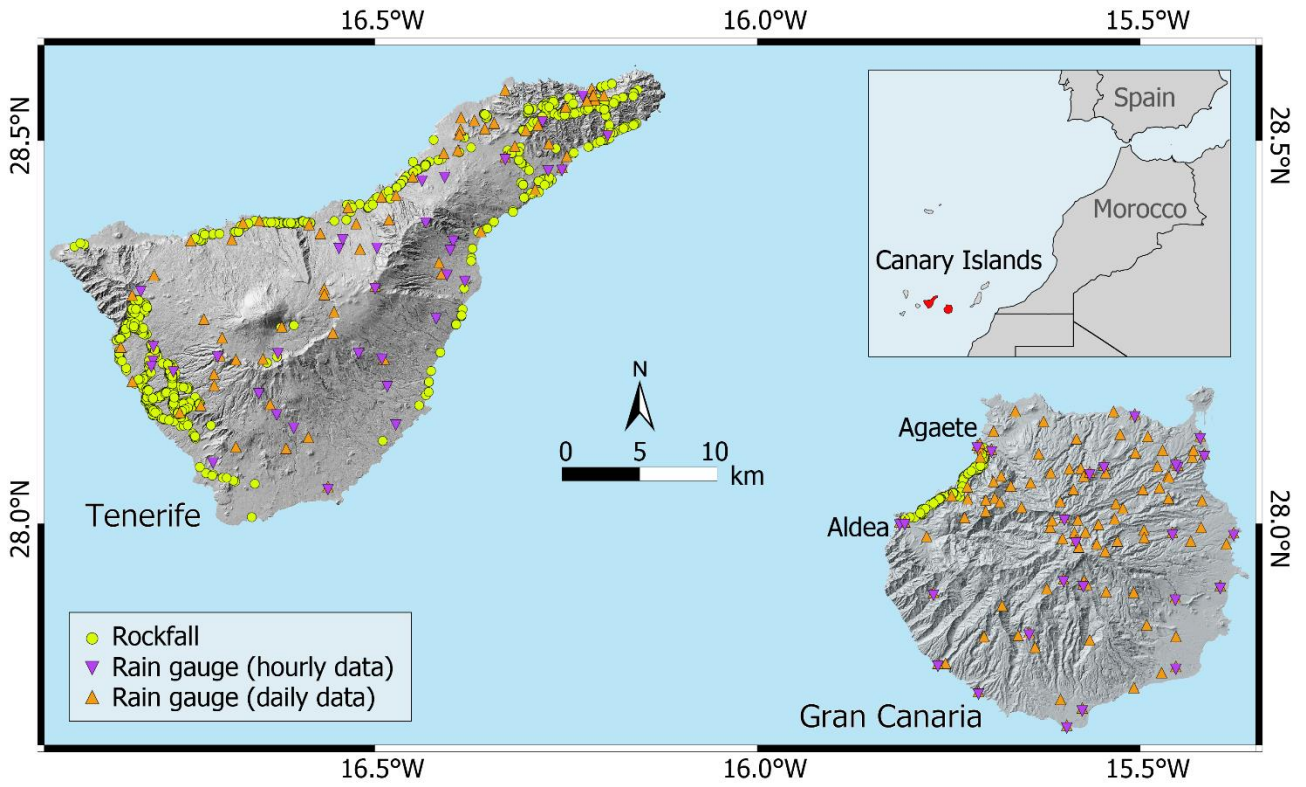
522

523 Figure 1. GC and TEN test sites. Location of the rain gauges providing hourly (purple triangles) and daily

524 (orange triangles) rainfall measurements, and of rockfalls used for threshold calculations (light green dots).

525 Hillshade derived from MDT05 2009 CC-BY 4.0 scne.es.

526

527   Figure 2. Photos of rockfalls in GC (a) and TEN (b) test sites (credits R.M. Mateos and S. Leyva Campos).

528

529
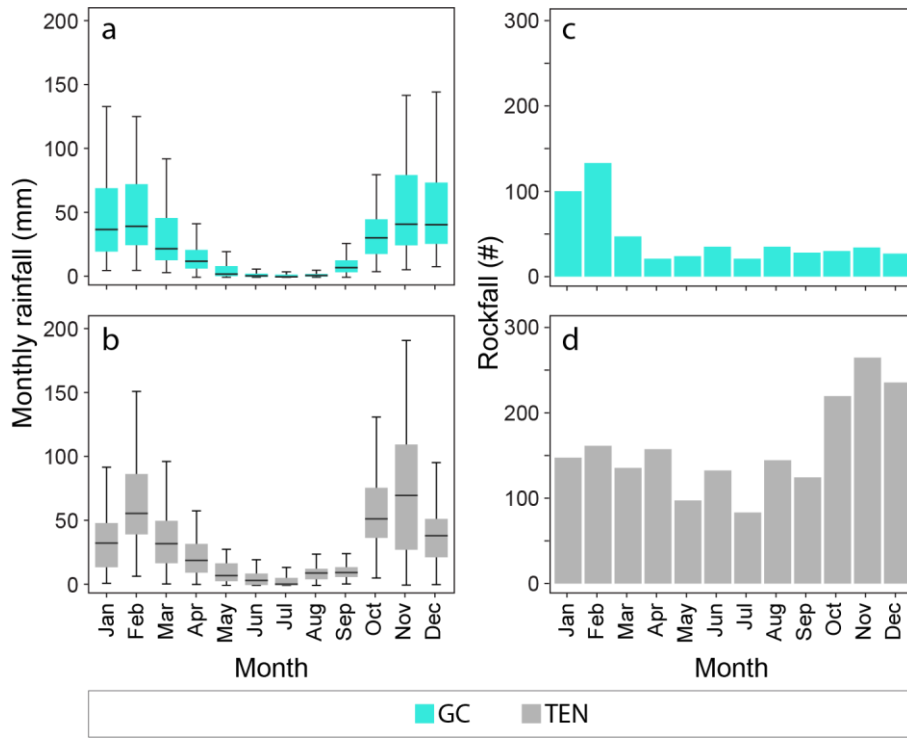
Figure 3. Comparison between monthly rainfall and rockfall occurrence. (a, b) Annual variation of monthly rainfall measures in GC (cyan) and TEN (grey). The whiskers show 1.5 times the interquartile range. (c, d) Number of rockfalls per month in the two test sites.
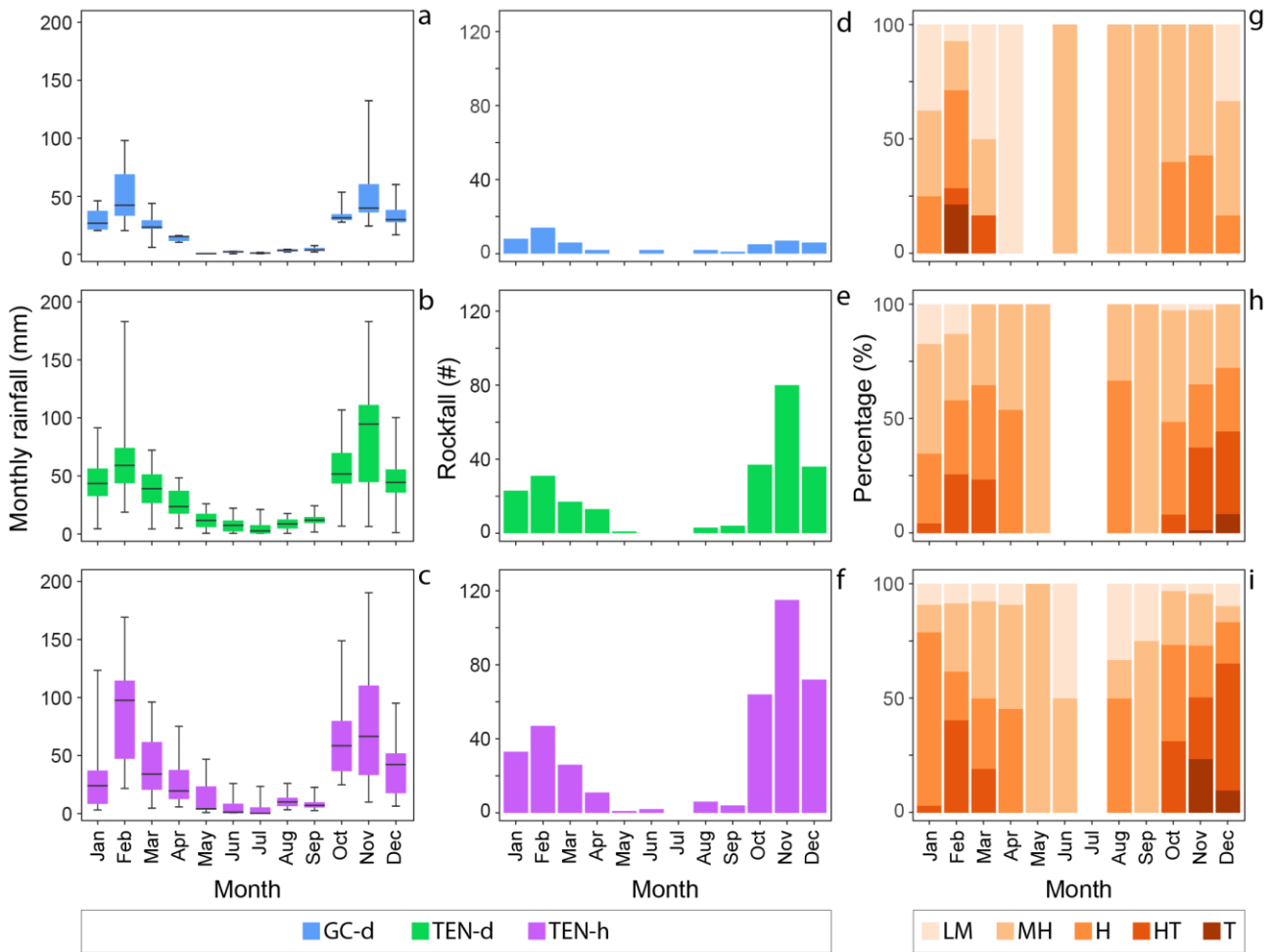
Figure 4. Comparison between monthly rainfall and rainfall-induced rockfalls and Alpert classification. (a, b, c) Annual variation of monthly rainfall measures in the test sites. Legend: GC-d, daily rainfall data in GC test site; TEN-d, daily rainfall data in the TEN test site; TEN-h, hourly rainfall data in TEN test site. (d, e, f) Number of rainfall-induced rockfalls per month. (g, h, i) Cumulated percentage of rainfall events per month classified according to Alpert et al. (2002). Legend: LM, light-moderate ($4 < E_d \leq 16$ mm); MH, moderate-heavy ($16 < E_d \leq 32$ mm); H, heavy ($32 < E_d \leq 64$ mm); HT, heavy-torrential ($64 < E_d \leq 128$ mm); T, torrential ($E_d > 128$ mm).

541
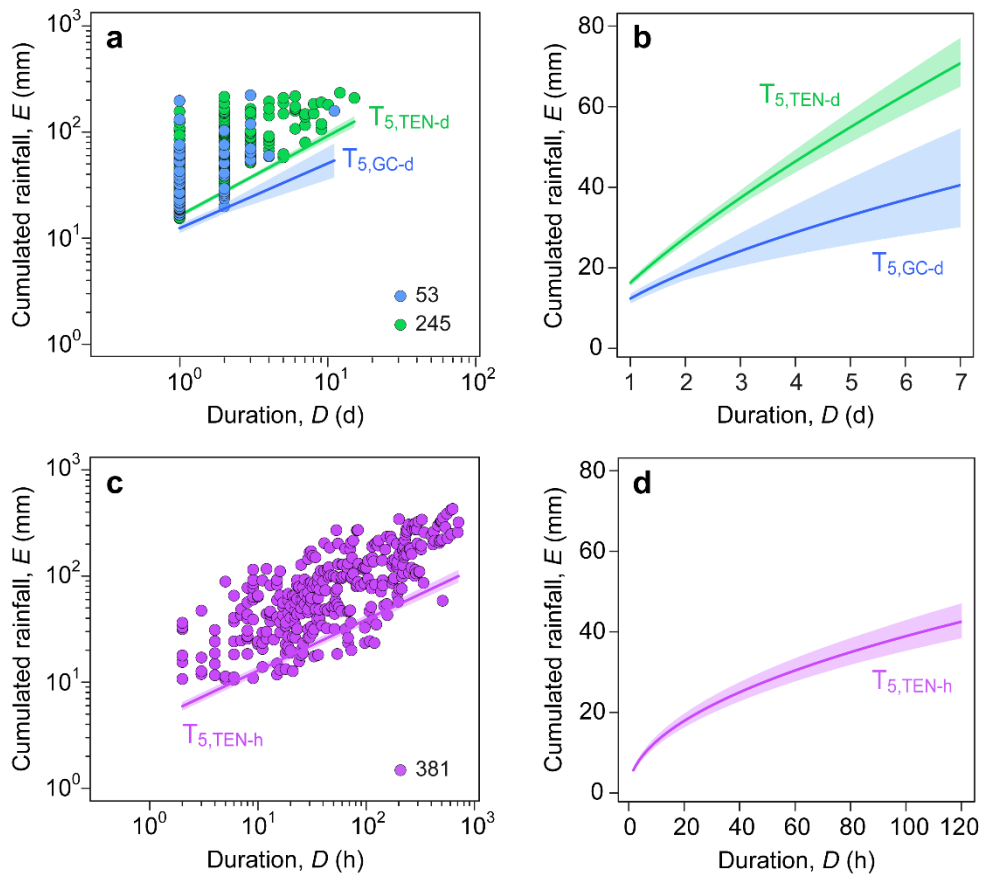
Figure 5. Rainfall thresholds for the possible rockfall occurrence in the two test sites. (a) Rainfall duration D (x-axis, in days) and cumulated event rainfall E (y-axis, in mm) conditions that have produced rockfalls in GC (53 blue dots) and TEN (245 green dots) test sites, respectively. Green and blue curves are the 5% power law thresholds ($T_{5,TEN-d}$, $T_{5,GC-d}$). (b) 5% daily ED thresholds for GC and TEN in linear coordinates, in the range of durations $1 \leq D \leq 7$ days. (c) Rainfall duration D (x-axis, in hours) and cumulated event rainfall E (y-axis, in mm) conditions that have produced rockfalls in TEN (381 purple dots) test site. Purple curve is the 5% power law threshold ($T_{5,TEN-h}$). (d) 5% hourly ED thresholds for GC and TEN in linear coordinates, in the range of durations $1 \leq D \leq 120$ hours.
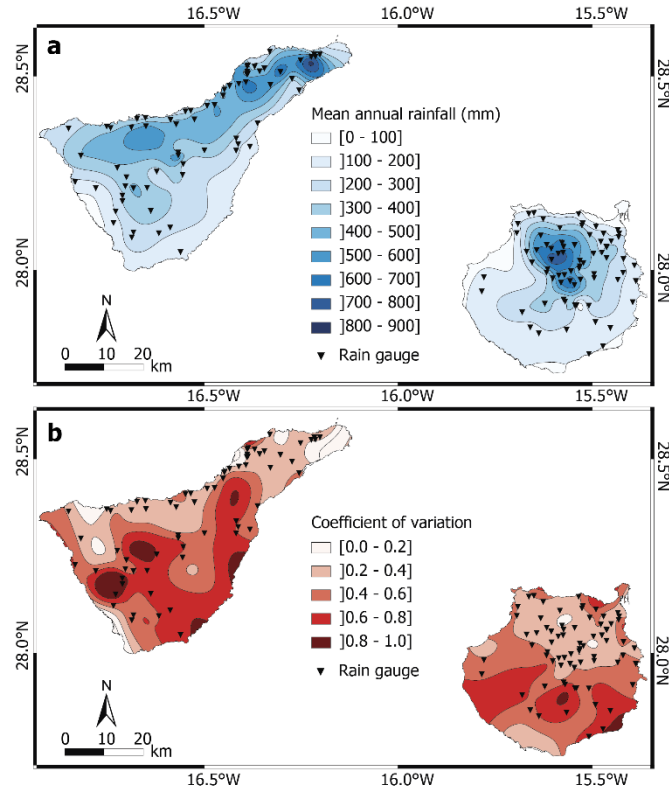
550

551   Figure 6. Maps of (a) mean annual rainfall and (b) of its coefficient of variation. The rain gauges used for these

552   analysis (cf. Table 1) are also shown.

553 Table 1. Summary of the three available rain gauge networks (CIAGC, AEMET, SIAR) in the two test sites

554 (GC and TEN) i.e., network name, network operating time period, temporal resolution, test site, number of

555 used rain gauges, their average operating time, and the use of data.

Network	Period	Temporal resolution	Test site	Rain gauges (#)	Average operating time (year)	Data application
CIAGC	Jan 2010 - Dec 2017	daily	GC	13	8.0	Thresholds
AEMET	Jan 1951 - May 2019			92	41.8	
	Oct 1997 - May 2019	hourly	GC	25	16.5	
	Jan 2010 - Mar 2018		TEN	34	5.5	
	Jan 2010 - May 2018	daily	TEN	66	8.2	
	Jan 2000 - Dec 2019	yearly	GC	67	15.2	MAR
			TEN	58	13.8	
SIAR	Jan 1999 - Dec 2019	monthly	GC	5	18.2	
			TEN	9	15.1	

556

557   Table 2. Summary of the number (#) and percentage (%) of MPRC in the categories proposed by Alpert et al.

558   (2002), in the two test sites.

Category	E_d (mm)	GC-d		TEN-d		TEN-h	
		#	%	#	%	#	%
Light (L)	$E_d \leq 4$	0	0	0	0	0	0
Light-moderate (LM)	$4 < E_d \leq 16$	11	20.7	11	4.5	28	7.3
Moderate-heavy (MH)	$16 < E_d \leq 32$	23	43.4	92	37.5	86	22.6
Heavy (H)	$32 < E_d \leq 64$	14	26.4	80	32.7	117	30.7
Heavy-torrential (HT)	$64 < E_d \leq 128$	2	3.8	58	23.7	116	30.5
Torrential (T)	$E_d > 128$	3	5.7	4	1.6	34	8.9

559

560

561   Table 3. *ED* rainfall thresholds at different non-exceedance probabilities (1%, 5%, 10%, 20%, 35% and 50%)

562   for the GC and TEN test sites. The number of MPRC and the duration range of each threshold are also reported.

Threshold name	Number of MPRC	Threshold equation	Duration range
$T_{1,GC-d}$		$E = (8.3\pm1.0)\times D^{(0.62\pm0.10)}$	
$T_{5,GC-d}$		$E = (12.3\pm1.2)\times D^{(0.62\pm0.10)}$	
$T_{10,GC-d}$	53	$E = (15.1\pm1.4)\times D^{(0.62\pm0.10)}$	1-11 days
$T_{20,GC-d}$		$E = (19.5\pm1.8)\times D^{(0.62\pm0.10)}$	
$T_{35,GC-d}$		$E = (25.5\pm2.5)\times D^{(0.62\pm0.10)}$	
$T_{50,GC-d}$		$E = (31.9\pm3.6)\times D^{(0.62\pm0.10)}$	
$T_{1,TEN-d}$		$E = (11.6\pm0.6)\times D^{(0.75\pm0.05)}$	
$T_{5,TEN-d}$		$E = (16.3\pm0.8)\times D^{(0.75\pm0.05)}$	
$T_{10,TEN-d}$	245	$E = (19.6\pm0.8)\times D^{(0.75\pm0.05)}$	1-15 days
$T_{20,TEN-d}$		$E = (24.4\pm1.0)\times D^{(0.75\pm0.05)}$	
$T_{35,TEN-d}$		$E = (30.6\pm1.4)\times D^{(0.75\pm0.05)}$	
$T_{50,TEN-d}$		$E = (37.1\pm1.8)\times D^{(0.75\pm0.05)}$	
$T_{1,TEN-h}$		$E = (2.8\pm0.3)\times D^{(0.48\pm0.02)}$	
$T_{5,TEN-h}$		$E = (4.3\pm0.4)\times D^{(0.48\pm0.02)}$	
$T_{10,TEN-h}$	381	$E = (5.3\pm0.5)\times D^{(0.48\pm0.02)}$	2-712 hours
$T_{20,TEN-h}$		$E = (6.9\pm0.6)\times D^{(0.48\pm0.02)}$	
$T_{35,TEN-h}$		$E = (9.1\pm0.7)\times D^{(0.48\pm0.02)}$	
$T_{50,TEN-h}$		$E = (11.4\pm1.0)\times D^{(0.48\pm0.02)}$	

563